Journal of Energy Chemistry 65 (2022) 194–204

Contents lists available at ScienceDirect

Journal of Energy Chemistry

journal homepage: www.elsevier.com/locate/jechem

http://www.journals.elsevier.com/journal-of-energy-chemistry/

Utilizing 3,4-ethylenedioxythiophene (EDOT)-bridged non-fullerene acceptors for efficient organic solar cells

Sung Jae Jeon [a,b], Young Hoon Kim [a], Ie Na Kim [a], Nam Gyu Yang [a], Ji Hee Yun [a], Doo Kyung Moon [a,*]

[a] Nano and Information Materials (NIMs) Laboratory, Department of Chemical Engineering, Konkuk University, 120 Neungdong-ro Gwangjin-gu, Seoul 05029, South Korea
[b] Department of Academy of Applied Science and Technology, Konkuk University, 120 Neungdong-ro Gwangjin-gu, Seoul 05029, South Korea

ARTICLE INFO

Article history:
Received 24 March 2021
Revised 10 May 2021
Accepted 23 May 2021
Available online 28 May 2021

Keywords:
Non-fullerene acceptor
3,4-ethylenedioxythiophene
Organic solar cell
π-bridge
π-spacer

ABSTRACT

A rational design of efficient low-band-gap non-fullerene acceptors (NFAs) for high-performance organic solar cells (OSCs) remains challenging; the main constraint being the decrease in the energy level of the lowest unoccupied molecular orbitals (LUMOs) as the bandgap of A-D-A-type NFAs decrease. Therefore, the short current density (J_{sc}) and open-circuit voltage (V_{oc}) result in a trade-off relationship, making it difficult to obtain efficient OSCs. Herein, three NFAs (IFL-ED-4F, IDT-ED-4F, and IDTT-ED-2F) were synthesized to address the above-mentioned issue by introducing 3,4-ethylenedioxythiophene (EDOT) as a π-bridge. These NFAs exhibit relatively low bandgaps (1.67, 1.42, and 1.49 eV, respectively) and upshifted LUMO levels (-3.88, −3.84, and −3.81 eV, respectively) compared with most reported low-band-gap NFAs. Consequently, the photovoltaic devices based on IDT-ED-4F blended with a PBDB-T donor polymer showed the best power conversion efficiency (PCE) of 10.4% with a high J_{sc} of 22.1 mA cm^{-2} and V_{oc} of 0.884 V among the examined NFAs. In contrast, IDTT-ED-4F, which was designed with an asymmetric structure of the D-π-A type, showed the lowest efficiency of 1.5% owing to the poor morphology and charge transport properties of the binary blend. However, when this was introduced as the third component of the PM6:BTP-BO-4Cl, complementary absorption and cascade energy-level alignment between the two substances could be achieved. Surprisingly, the IDTT-ED-4F-based ternary blend device not only improved the J_{sc} and V_{oc}, but also achieved a PCE of 15.2%, which is approximately 5.3% higher than that of the reference device with a minimized energy loss of 0.488 eV. In addition, the universality of IDTT-ED-2F as a third component was effectively demonstrated in other photoactive systems, specifically, PM6:BTP-eC9 and PTB7-Th:IEICO-4F. This work facilitates a better understanding of the structure–property relationship for utilizing efficient EDOT-bridged NFAs in high-performance OSC applications.

1. Introduction

The active layer of solution-processed bulk-heterojunction (BHJ) organic solar cells (OSCs) contains light-absorbing organic semiconductors, which are generally composed of polymers and small molecules that act as electron donors and acceptors, respectively [1]. Much effort has been made to optimize the light absorption, energy level, and charge transport properties of donor polymers so that they match well with fullerene derivatives, which are representative electron acceptors. However, it has been extremely difficult to obtain OSCs with an efficiency over 10% solely by developing a proper donor material [2–4]. Therefore, many researchers have focused on developing various forms of non-fullerene acceptor (NFA) derivatives to replace fullerene by overcoming the synthetic inflexibility of fullerene (e.g., constraints including the frontier energy-level control and poor absorption in the visible to near infrared (NIR) region) [5–7]. In 2015, Zhan et al. developed a 1.59-eV low-band-gap A-D-A type NFA, namely, 3,9-bis(2-methylene-(3-(1,1-dicyanomethylene)-indanone))-5,5,11,11-tetrakis(4-hexylphenyl)-dithieno[2,3-d:2′,3′-d′]-s-indaceno[1,2-b:5,6-b′]dithiophene (ITIC), which is composed of indacenodithieno[3,2-b]thiophene as the donor (D) core and 2-(3-oxo-2,3-dihydroinden-1-ylidene)malononitrile as the strong acceptor (A). It exhibited a high potential by reaching an efficiency comparable to that of a fullerene-based OSC device [8]. In the following year, Hou et al. combined this material with a wide-bandgap donor polymer, namely, poly[(2,6-(4,8-bis(5-(2-ethylhexyl)thiophen-2-yl)-benzo[1,2-b:4,5-b′]dithiophene))-alt-(5,5-(1′,3′-di-2-thienyl-5′,7′-bis(2-ethylhexyl)benzo[1′,2′-c:4′,5′-c′]dithio

* Corresponding author.
E-mail address: dkmoon@konkuk.ac.kr (D.K. Moon).

https://doi.org/10.1016/j.jechem.2021.05.032

phene-4,8-dione))] (PBDB-T), which acted as a counterpart of the ITIC. They reported an efficiency of over 11%, after which the performance of the OSCs improved rapidly [9]. In 2019, Zou et al. transformed the D in the A-D-A building block to a fused DA'D core and developed a new A-DA'D-A-type NFA, namely, 2,2′-((2Z,2′Z)-((12,13-bis(2-ethylhexyl)-3,9-diundecyl-12,13-dihydro-[1,2,5]-thiadiazolo[3,4-e]thieno[2″,3″:4′,5′]thieno[2′,3′:4,5]pyrrolo[3,2-g]thieno[2′,3′:4,5]thieno[3,2-b]indole-2,10-diyl)bis(methanylylidene))bis(5,6-difluoro-3-oxo-2,3-dihydro-1H-indene-2,1-diyli dene))dimalononitrile (Y6), which can form an upshifted lowest unoccupied molecular orbital (LUMO) level and ultra-low bandgap of 1.33 eV with a more effective push–pull system than prior systems. A remarkable device performance of over 15% was achieved based on poly[(2,6-(4,8-bis(5-(2-ethylhexyl-3-fluoro)thiophen-2-yl)-benzo[1,2-b:4,5-b']dithiophene))-alt-(5,5-(1′,3′-di-2-thienyl-5′,7′-bis(2-ethylhexyl)benzo[1′,2′-c:4′,5′-c']dithiophene-4,8-dione)] (PM6) [10–13]. According to the latest literature, the efficiency of OSCs is expected to exceed 20% in the near future with the development of optimizing morphology technology, as well as enhanced donor and acceptor molecular structures [14,15].

Continuous efforts to develop efficient NFAs and understand their structure–property relationship in terms of improved light absorption, as well as the ease of frontier energy-level engineering, play a key role in the development of OSCs [16]. For the efficient development of OSCs, the absorption profiles between photoactive components should be matched carefully to provide wide-ranging external quantum efficiency (EQE) responses and a relatively high short-circuit current while contributing to efficient charge generation. Because most low-bandgap NFAs have a lower electron affinity than fullerene, wide-bandgap donors should be used in pairs to improve the open-circuit voltage. Next, the LUMO energy level should be changed and optimized according to the specific target donor polymers. Furthermore, the energy loss (E_{loss}) in electron transfer should be minimized, and the highest possible internal voltage should be guaranteed [17]. Typical NFAs of the A-D-A type can be achieved by combining electron-rich and electron-deficient structural units. Hence, the absorption can be expanded, and the separation of the HOMO and LUMO electrons can be controlled by reducing the optical bandgap through molecular orbital hybridization. In addition, designing the molecular structure of the A-π-D-π-A-type using π-bridges (π-spacers) enables more detailed and effective control [18]. For example, when thiophene is introduced into the A-π-D-π-A skeleton as a general π-bridge, both the HOMO and LUMO levels are upshifted and a lower bandgap can be obtained [19]. However, the introduction of a π-bridge sometimes increases the structural uncertainty and causes changes in the solubility, crystallinity, and orientation characteristics. Therefore, it is extremely difficult to simultaneously increase both V_{oc} and J_{sc} in an OSC device.

To address this issue, several methods have been successfully developed, including the introduction of oxygen-substituted thiophene derivatives as π-bridges. In 2018, Bo et al. announced NFAs for ITOIC, ITOIC-2F, and ITOIC-2F with 1.45-eV-or-lower bandgaps by introducing 3,4-bis(hexyloxy)thiophene as a π-bridge [20]. All three types had a highly planar backbone with noncovalent conformational locking via S···O and O···H interactions between the D and A units adjacent to the π-bridge, and they exhibited high π − π stacking properties. The PBDB-T-based device with the ITOIC-2F blend showed an excellent performance of 12.17% with a relatively high V_{oc} of 0.897 V and J_{sc} of 21.04 mA/cm^2. In the same year, Bo et al. developed IDT-PDOT and IDT-EDOT, which are low-bandgap NFAs with a maximum bandgap of 1.41 eV. They achieved these systems using 3,4-propylenedioxythiophene (PDOT) and 3,4-ethylenedioxythiophene (EDOT) as bridging units interconnecting D and A [21]. According to the result of a device optimized for the PBDB-T donor, IDT-EDOT achieved a high efficiency of 11.32% with a V_{oc} of 0.86 V and a J_{sc} of 21.34 mA/cm^2, whereas IDT-PDOT achieved a very low efficiency of 2.18% with a V_{oc} of 0.85 V and a J_{sc} of 5.26 mA/cm^2. The cause appears to be the fact that, compared to the IDT-EDOT with EDOT in the form of a hexagonal ring, introducing a PDOT bridge in the form of a heptagonal ring into the backbone tilted the dihedral angle with the adjacent acceptor unit by approximately 7°, resulting in relatively poor π − π stacking. Therefore, the use of a π-bridge that causes noncovalent interactions in the molecular structure is key for the development of efficient NFAs.

In this study, three types of NFAs with different bandgaps of 1.67, 1.42, and 1.49 eV, i.e., IFL-ED-4F, IDT-ED-4F, and IDTT-ED-2F, respectively, were successfully developed using EDOT. This material can maintain a high-planar backbone via noncovalent conformational locking between adjacent moieties and form an upshifted LUMO level while effectively reducing the bandgap as a π-bridge. In addition, OSC devices were produced by matching with photoactive layer materials such as PBDB-T, PM6, and 2,2′-((2Z,2′Z)-((12,13-bis(2-butyloctyl)-3,9-diundecyl-12,13-dihydro-[1,2,5]thiadiazolo[3,4-e]thieno[2″,3″:4′,5′]thieno[2′,3′:4,5]pyrrolo[3,2-g]thieno[2′,3′:4,5]thieno[3,2-b]indole-2,10-diyl)bis(methanylylidene))bis(5,6-dichloro-3-oxo-2,3-dihydro-1H-indene-2,1-diyli dene))dimalononitrile (BTP-BO-4Cl) (see the molecular structures given in Chart 1). We discovered several crucial factors affecting the utilization of EDOT materials for the efficient design of NFAs. First, if the EDOT bridge is bridged with a terminal thiophene ring such as indacedenothiophene (IDT) and indacenodithienothiophene (IDTT), a high planarity is maintained with a dihedral angle of $\leq 1°$, whereas if it is bridged with a benzene ring such as indacenofluorene (IFL), the NFA exhibits a large tilt of $\geq 20°$. Second, the general Knoevenagel condensation reaction of IDT-ED-4F formed byproducts or isomers. This issue allowed us to obtain fully controlled, highly pure products by synthesizing using an improved and more rational synthetic route. Lastly, the high potential of the D-π-A-type NFA, IDT-ED-2F, which has not yet been reported, was observed when it was used as a ternary compound. In summary, the device test results of PBDB-T and NFAs for IFL-ED-4F, IDT-ED-4F, and IDTT-ED-2F showed PCEs of 7.5%, 10.4%, and 1.5%, respectively, thereby indicating that IDTT-ED-2F had the lowest performance. However, when 10 wt% of NFAs were introduced as a third component of the PM6 and BTP-BO-4Cl combination, the results showed enhanced PCEs of 14.7%, 14.4%, and 15.2%, respectively, compared to the reference PCE of 14.4%. In contrast to binary blend systems, IDTT-ED-2F had the best performance among the NFAs. To investigate the correlations with the photocell properties, physical, optical, electrochemical, and crystallographic analyses were conducted systematically and carefully. This demonstration suggests that the strategy of using EDOT as a π-bridge for efficient NFA design is a highly useful method and provides much information in terms of molecular structure design.

2. Results and discussion

2.1. Material design and synthesis, physical properties, and theoretical calculations

The syntheses of the new EDOT-bridged NFAs for IFL-ED-4F, IDT-ED-4F, and IDTT-ED-2F are described in Scheme 1. The detailed synthesis processes and yields are provided in the Supplementary Information (SI). The chemical structure of each new chemical was fully characterized by ^{1}H NMR, ^{13}C NMR, and MALDI-TOF (Figs. S1–S11). It should be noted that synthetic routes 1 and 2 (R1 and R2) were used to synthesize IDT-ED-4F. When the final Knoevenagel condensation reaction was performed using the typical synthetic route R1, only IFL-ED-4F formed the major product, while IDT-

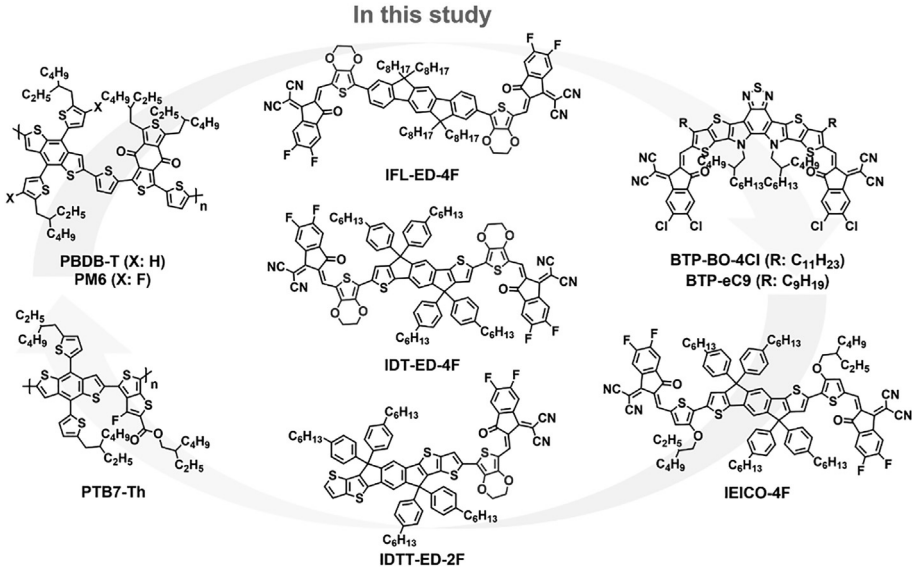

Scheme 1. Synthetic routes (R1 and R2) to EDOT-bridged NFAs: IFL-ED-4F, IDT-ED-4F, and IDTT-ED-2F.

ED-4F formed two or more byproducts or isomers. As shown in Fig. S12, it is very difficult to selectively isolate the product when refining via silica-gel-loaded column chromatography with a chloroform eluent. As a result, R1-M4 (IDT-ED-4F) was obtained with a low yield of 45% and a low purity (two steps and a yield of 34.4% in total). However, this problem can be completely solved using the synthetic route R2. More specifically, the Knoevenagel condensation of the EDOT bridge was performed first with the 2-(5,6,-difluoro-3-oxo2,3-dihydro-1H-inden-1-ylidene)malononitrile (2F-IC) end group as the acceptor before finally synthesizing the product through the Stille C–C coupling reaction with the target core donor unit. In the case of R1, when the EDOT bridge is linked to the IDT core with a stronger quinoidal structure than the IFL core during Knoevenagel condensation, the probability of creating a mesomerically unstable electronic environment is increased, thereby causing side reactions as radicals easily escape under a strong base [22]. In contrast, R2 can obtain an intermediate product with a high yield close to 100% using an alcoholic solvent—a more environmentally friendly solvent without using a base for Knoevenagel condensation. This method can effectively prevent the problem of the conventional R1 pathway. Furthermore, it has the advantage of saving costs because the 2F-IC end group unit consumes only one equivalent, which is lower than that of the existing R1 pathway. As a result, as shown in Fig. S13, R2-M2 (IDT-ED-4F) (two steps and a yield of 95.0% in total) can achieve a high yield of 95% and a high purity. Finally, IDTT-ED-2F, a D-π-A-type NFA with an asymmetric structure, was synthesized by the same method, and achieved a high yield of 91% by limiting the equivalent ratio of R2-M1 to one. In addition, the EDOT bridge could be effectively applied with other end group structures. As shown in Figs. S14 and S15, barbituric acid (BA) and rhodanine (Rh) have been successfully combined with EDOT bridge as weaker electron-withdrawing end groups than 2F-IC. The overall yields of both reactions were over 90%; Rhodanine derivative only requires 1–2 droplets of piperidine under the same conditions. The results indicate that EDOT bridges with diverse electronic systems can be easily utilized as tools for designing efficient NFAs. The synthesized three NFAs exhibit good solubility in common organic solvents such as methylene chloride, tetrahydrofuran, and chloroform. The results of thermogravimetric analysis (TGA) confirmed that the decomposition temperature T_d (i.e., the temperature at which a 5% sample weight loss occurred) for each NFA was above 295 °C. This implies that all three structures have the sufficient thermal stability required for organic electronic applications such as OSCs (Fig. S16). The crystalline natures of the molecular structures were examined by differential scanning calorimetry (DSC) [23] (Fig. S17). First, IFL-ED-4F showed a crystalline temperature (T_c) of 155.75 °C, and the crystallization enthalpy (H_c) was found to be 5.90 J g^{-1}, whereas IDT-ED-4F showed no obvious thermal transitions between 25 and 250 °C. Interestingly, IDTT-ED-2F did not demonstrate a T_c, and only a melting temperature (T_m) of 200.17 °C was observed with a melting enthalpy (H_m) of 11.74 g^{-1}. It seems that IDTT-ED-2F with an asymmetric D-π-A structure formed very small crystals that were not detectable in the DSC analysis, and heat was then emitted as a phase transition occurred near 200 °C [24]. The fact that the melting temperature is below 250 °C suggests that the D-π-A structure is thermodynamically unstable compared to A-π-D-π-A structures [25]. Details of the measured results are summarized in Table 1.

Considering the potential use of EDOT as a π-bridge, density functional theory (DFT) calculations of the π-A structures together with methoxy(in/out)- and dimethoxy-substituted thiophene, which have similar properties, was performed at the B3LYP/6–31G(d,p) level of the Gaussian 09 package. As shown in Figs. S18 and S19, the optimal geometric configurations of Me(in/out)OT-2F, DMOT-2F, and EDOT-2F showed high planarity with 2F-IC as they exhibited a dihedral angle close to 0°, but they showed significant differences in their frontier energy levels and dipole moments. The calculation results show that the ascending order of the bandgap is Me(in)OT-2F, Me(out)OT-2F, EDOT-2F, and 2MeOT-2F, whereas the descending order of the LUMO level is Me(out)OT-2F, EDOT-2F, Me(in)OT-2F, and 2MeOT-2F. It is crucial to form an upshifted LUMO level and a low bandgap for efficient NFAs. Furthermore, they must have a high dipole moment to aid and boost the charge carrier separation at the D-A interfaces [26]. Therefore, the EDOT-2F combination appears to be the best material among the π-A structures. The detailed values obtained by the DFT calculations are summarized in Table S1.

More precise computing simulations were performed with the same structures as the synthesized NFAs for IFL-ED-4F, IDT-ED-4F, and IDTT-ED-2F. These calculations were simplified by replacing long alkyl chains with methyl groups to reduce computational consumption. As shown in Fig. S20, IDT-ED-4F and IDTT-ED-2F showed high planarity because they have very small dihedral

Table 1
Physical, optical, and electrochemical properties of NFAs.

NFAs	Physical properties (TGA and DSC)	Optical properties(UV)				Electrochemical properties(CV)			
	$T_d^{a)}$[°C]	Solution λ_{max} [nm]	ε [M^{-1} cm^{-1}]at λ_{max} [nm]	Film λ_{max} [nm]	$E_g^{opt,\ b)}$[eV]	E_{ox}^{onset}[V]	$E_{HOMO}^{c)}$[eV]	E_{red}^{onset}[V]	$E_{LUMO}^{c)}$[eV]
IFL-ED-4F	419	320,368,637	46,619 (320),45,657 (368), 152,672 (637)	380,651	1.67	1.37	−5.71	−0.50	−3.84
IDT-ED-4F	373	309,751	33,204 (309),173,719 (751)	315,785	1.42	1.04	−5.38	−0.46	−3.88
IDTT-ED-2F	295	399,711	22,120 (399),85,585 (711)	405,727	1.49	1.13	−5.47	−0.53	−3.81

a) Temperature resulting in a weight loss of 5% of the initial weight.
b)Calculated from the intersection of the tangent on the low-energy edge of the absorption spectrum with the baseline. c) E HOMO or LUMO = −4.8 − [E ox or red onset (vs. Ag/AgCl) − E 1/2(Fc/Fc + vs. Ag/AgCl)] (E 1/2(Fc/Fc + vs. Ag/AgCl) = 0.46 eV).

angles of 0° and 1° for θ_1, θ_2, θ_3, and θ_4 with the introduction of the EDOT bridge. In contrast, IFL-ED-4F showed relatively low planarity because it has a large tilting angle of 20.5° for θ_2 and θ_3. This is because there are differences in the interactions between atoms with noncovalent conformational locking between the EDOT bridge and different donor cores [27,28]. More specifically, IDT and IDTT can perform S···O and O···H interactions with adjacent EDOT, but IFL can only perform O···H interactions. Therefore, selecting donor core units with heterocyclic rings that can have double locking on both ends can be important when designing high-planar EDOT-bridged NFAs. The calculated frontier energy levels showed that the bandgap decreased in the order of IFL-ED-4F, IDTT-ED-2F, and IDT-ED-4F, whereas the LUMO level increased in the order of IDT-ED-4F, IFL-ED-4F, and IDTT-ED-2F. In particular, the IDTT-ED-2F of the D-π-A type had a weaker push–pull system than IFL-ED-4F and IDT-ED-4F of the A-π-D-π-A structure, and it showed the highest LUMO level because of its relatively weak electron-withdrawing property. Finally, the charge transfer properties of the NFAs were compared from the perspective of chemical structure through the analysis of electrostatic potential (ESP), as shown in Fig. 1. First, it is notable that all the three NFAs have partially a strong positive charge on the ethylene of the OT-bridge and a strong negative charge on the oxygen and nitrogen of the flanked end group. Therefore, it can be predicted that fast charge transport is possible in the conjugated backbone by electrostatic forces [29,30]. Considering the dipole moment, IDT-ED-4F with a symmetric structure and a high-planar backbone showed the lowest value, followed by IFL-ED-4F with the EDOT bridge adjacent to the donor core, and IDTT-ED-2F with an asymmetric structure showed the highest dipole moment. Therefore, if a sufficient intermolecular electric field is formed when the donor polymer comes into contact with the NFAs, more efficient charge transport is possible with a larger dipole moment [30,31]. The detailed values obtained by DFT calculations are summarized in Table S2.

2.2. Optical and electrochemical properties

The optical and electrochemical properties of EODT-bridged NFAs for IFL-ED-4F, IDT-ED-4F, and IDTT-ED-2F were investigated via UV–vis spectroscopy and cyclic voltammetry (CV), as shown in Fig. 2. All EDOT-bridged NFAs typically exhibited two clear absorption bands at approximately 300 to 450 nm and 600 to 900 nm, corresponding to the π–π* transition and intramolecular charge transfer (ICT), respectively. These are complementary to the PBDB-T and PM6 donor polymers, which have a strong absorption band in the range of 500 to 650 nm [20,21].

As shown in Fig. 2a, distinct shoulder peaks were observed at approximately 640 and 750 nm for both IFL-ED-4F and IDT-ED-4F of the A-π-D-π-A structure, and the solution exhibited self-organization properties; however, such aggregation behavior was not observed in IDTT-ED-2F of the D-π-A structure. The molar absorption coefficients (ε) of the NFAs were calculated from the UV–vis data on chloroform solutions with different concentrations on the order of 10^{-5} M and the Beer–Lambert equation [32,33]. As a result, the maximum ε values of IFL-ED-4F and IDT-ED-4F were 1.52×10^5 M^{-1} cm^{-1} and 1.73×10^5 M^{-1} cm^{-1}, respectively, which are similar to or slightly higher than those of the NFAs reported in the literature [10,11,20,21]. However, owing to the lack of the π-A structure on one side, IDTT-ED-2F exhibited an ε value of 8.55×10^4 M^{-1} cm^{-1}, which is 1 magnitude lower than those of the other two NFAs. As shown in Fig. 2b, the NFAs of IFL-ED-4F, IDT-ED-4F, and IDTT-ED-2F in the film state showed significant

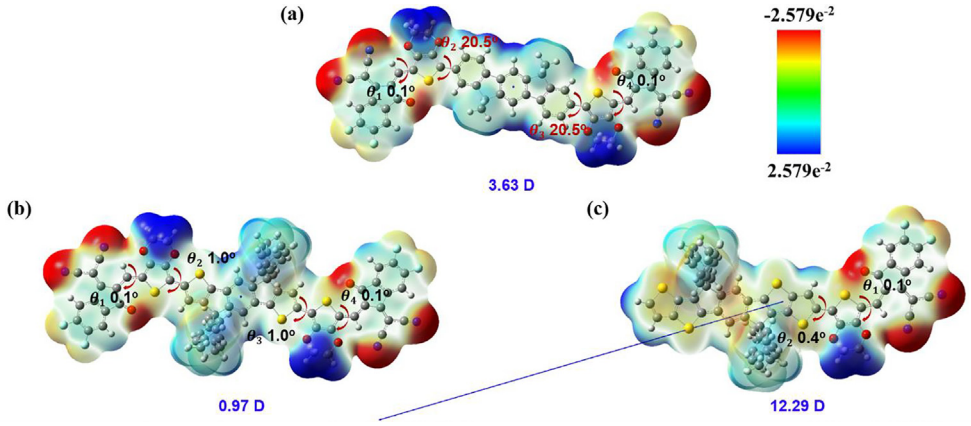

Fig. 1. Calculated ESP surfaces of EDOT-bridged NFAs: top views with dihedral angles (θ_1, θ_2, θ_3, and θ_4) and dipole moments for (a) IFL-ED-4F, (b) IDT-ED-4F, and (c) IDTT-ED-2F.

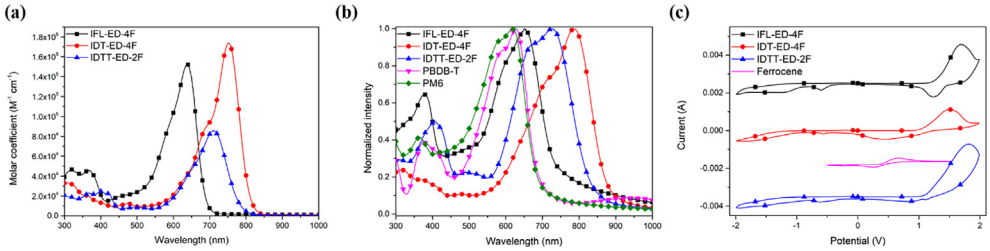

Fig. 2. UV–vis absorption spectra, CV curves, and energy band diagrams of EDOT-bridged NFAs: (a) average molar absorption coefficients in chloroform (measured using 10^{-5} M chloroform solutions), (b) UV–vis absorption spectra of thin films containing with PBDB-T and PM6 donor polymer, and (c) CV curves of thin films containing ferrocene.

red shifts with maximum absorption wavelengths of 14, 34, and 16 nm, respectively. This is associated with the degree of J-aggregate formation due to the close packing of the molecular structures in the solid state [34]. The optical bandgaps (E_g^{opt}) of IFL-ED-4F, IDT-ED-4F, and IDTT-ED-2F calculated at the onset of thin film absorption are 1.67, 1.42, and 1.49 eV, respectively, which is consistent with the trend of the computing simulation data. In particular, according to the solid-state absorption characteristics, the J_{sc} value of the NFAs may increase in the order of IDT-ED-4F, IDTT-ED-2F, and IFL-ED-4F, thereby indicating that they are capable of absorbing a wide range of light up to the NIR region. Moreover, as shown in Fig. S21a, all NFAs have the absorption wavelength band and complementary optical properties of PBDB-T and PM6 with a wide bandgap of 1.79 and 1.80 eV. Therefore, light harvesting can be improved over a wide spectrum extending from UV to NIR. Similarly, Three NFAs showed complementary absorption spectrum with PM6:BTP-BO-4Cl, which is a desirable combination for improving light harvesting via fabricating ternary OSCs.

Next, the frontier energy levels of NFAs can be calculated from the oxidation–reduction curve, as shown in Fig. 2c. The measured HOMO (E_{LUMO}) and LUMO energy levels (E_{HOMO}) of the NFAs were determined from the onset oxidation potential (E_{ox}^{onset}) and reduction potential (E_{red}^{onset}), respectively, and using the following electrochemical equation: $E_{HOMO\ or\ LUMO} = -4.8 - (E_{ox\ or\ red}^{onset} - E_{1/2,ferrocene})$, where $E_{1/2,ferrocene} = 0.46$ eV (measured data) [32,33,35]. As a result, the HOMO & LUMO levels of IFL-ED-4F, IDT-ED-4F, and IDTT-ED-2F are −5.71 & −3.84 eV, −5.38 & −3.88 eV, and −5.47 & −3.81 eV, respectively, which are in good agreement with the results of the DFT calculations except for the HOMO value of IDTT-ED-2F. Experimentally, the deeper HOMO level of IDTT-ED-2F with D-π-A structure suggests that actual electron clouds are distributed over the entire conjugated backbone and have a stable state [36]. As shown in Fig. S21b, it was expected that when the NFAs were blended with donor polymers such as PBDB-T and PM6, the frontier energy levels would be well aligned, which favors efficient charge transport. In addition, the open-circuit voltage (V_{oc}) increased in the following order: IDTT-ED-2F, IFL-ED-4F, and IDT-ED-4F. However, in the case of the IDT-ED-4F and PM6 combinations, there is a reversed HOMO offset of −0.07 eV between the HOMO levels. If the driving force is insufficient, the probability of charge recombination is expected to be high in this system [37,38]. The optical and electrochemical properties of the polymers are listed in Table 1.

2.3. Photovoltaic performance

The photovoltaic characteristics of the three NFAs were investigated in the inverted device structure of indium tin oxide (ITO)/zinc oxide (ZnO)/active layer/molybdenum oxide (MoO_3)/silver (Ag). Here, the active layer was a binary blend of a PBDB-T donor and NFAs, and it was optimized by varying the ratio, solvent, additive, and temperature. The optimization process is summarized in Tables S3–S5. The *J–V* characteristics and EQE of the optimized devices of the NFAs for PBDB-T:IFL-ED-4F, PBDB-T:IDT-ED-4F, and PBDB-T:IDTT-ED-2F are shown in Fig. 3a and 3b, and the detailed parameters are listed in Table 2.

First, in the case of IFL-ED-4F, the devices made of a solution of PBDB-T:IFL-ED-4F = 1:1 (wt/wt) chlorobenzene (CB) with 0.5 vol% diphenyl ether (DPE) showed a PCE of 7.5% with *a* V_{oc} of 0.939 V, J_{sc} of 13.6 mA cm^{-2}, and FF of 58.2%. A high efficiency of ≥ 10% could not be achieved because of the low J_{sc} value in contrast with the relatively high V_{oc}. This is because, as shown in the EQE curve, IFL-ED-4F overlapped with the absorption area of the PBDB-T polymer, and the yield of sunlight is limited and small compared to other NFAs. In contrast, IDT-ED-4F, which has the lowest bandgap (1.42 eV), is optically and electrochemically well-matched with the PBDB-T polymer, as reported in the literature [21].

Therefore, the device made of PBDB-T:IDT-ED-4F = 1:1 CB with a 0.2 vol% 1,8-diiodooctane (DIO) solution showed a maximum PCE of 10.4% with an outstanding J_{sc} of 22.1 mA cm^{-2}. In particular, as shown in the EQE curve, a broad range of PCEs from 300 to 900 nm was observed. Flat EQE values of approximately 75% were achieved near the maximized wavelengths of both the donor and acceptor, confirming the possibility of efficient light harvesting and charge collection. Finally, IDTT-ED-2F with a D-π-A structure showed the lowest PCE of 1.5% with a V_{oc} of 0.906 V, J_{sc} of 5.1 mA cm^{-2}, and FF of 31.8%, even though it has complementary light absorption properties and well-arranged frontier energy levels with the PBDB-T polymer. Organic chromophores of the D-π-A structure have been extensively researched as sensitizers for electron donors because they facilitate photoinduced charge separation in dye-sensitized solar cells (DSSCs) [39]. Therefore, to verify the potential of IDTT-ED-2F as a donor, a device was fabricated with CB by mixing it with a [6,6]-Phenyl-C71-butyric acid methyl ester ($PC_{71}BM$) acceptor at a ratio of 1:1 (wt/wt). As a result, it showed a much lower PCE of 0.4% with a V_{oc} of 0.801 V, J_{sc} of 1.9 mA cm^{-2}, and FF of 27.2%; thus, IDTT-ED-2F was found to be more efficient as an electron acceptor than an electron donor.

Generally, compatible energy levels of the donor and acceptor components are essential for highly efficient OSCs, which can ensure efficient charge separation and minimize E_{loss} [5–7,17]. As shown from the above CV analysis, the LUMO offset energy values between the donor and acceptor in the blends of PBDB-T and NFAs for IFL-ED-4F, IDT-ED-4F, and IDTT-ED-2F are 0.30, 0.34, and 0.27 eV, respectively. By contrast, the HOMO offset energy values for IFL-ED-4F, IDT-ED-4F, and IDTT-ED-2F are 0.38, 0.05, and 0.12 eV, respectively, which should be sufficient for exciton dissociation and charge transfer between the donor and acceptor [7,17]. Finally, energy loss (E_{loss}) is considered an important parameter in evaluating the photovoltaic performance of devices. E_{loss} can be estimated by the equation $E_{loss} = E_g^{opt} - eV_{oc}$, where E_g^{opt} is the smallest optical bandgap between the donor and acceptor [5–7,17]. As shown in Table 2, the E_{loss} values for IFL-ED-4F, IDT-ED-4F, and IDTT-ED-2F were calculated as 0.711, 0.540, and

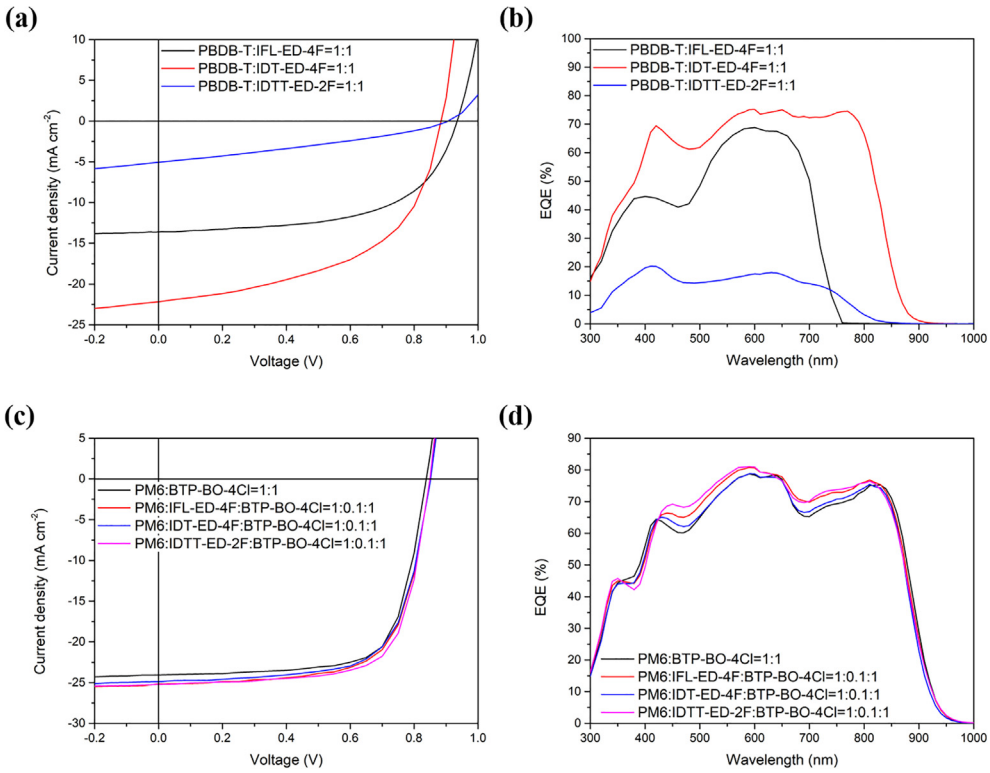

Fig. 3. (a, c) *J*–*V* and (b, d) EQE curves of the optimized blend devices: (a, b) PBDB-T:IFL-ED-4F, PBDB-T:IDT-ED-4F, and PBDB-T:IDTT-ED-2F; (c, d) PM6:BTP-BO-4Cl, PM6:IFL-ED-4F:BTP-BO-4Cl, PM6:IDT-ED-4F:BTP-BO-4Cl, and PM6:IDTT-ED-2F:BTP-BO-4Cl.

Table 2
Photovoltaic performance of NFAs-based OSCs for each optimized condition.

Active layer	V_{oc}[V]	J_{sc}[mA cm^{-2}]	FF[%]	PCE$_{max}$/PCE$^{a)}_{ave}$[%]	$E^{b)}_{loss}$[eV]
PBDB-T:IFL-ED-4F = 1:1	0.94	13.64	58.24	7.5/7.3±0.17	0.711
PBDB-T:IDT-ED-4F = 1:1	0.88	22.14	53.04	10.4/10.2±0.13	0.540
PBDB-T:IDTT-ED-2F = 1:1	0.91	5.10	31.75	1.5/1.2±0.27	0.560
PM6:BTP-BO-4Cl = 1:1	0.84	24.06	71.48	14.4/14.1±0.35	0.502
PM6:IFL-ED-4F:BTP-BO-4Cl = 1:0.1:1	0.85	25.23	68.54	14.7/14.5±0.20	0.489
PM6:IDT-ED-4F:BTP-BO-4Cl = 1:0.1:1	0.85	24.91	68.01	14.4/14.2±0.20	0.490
PM6:IDTT-ED-2F:BTP-BO-4Cl = 1:0.1:1	0.85	25.16	71.26	15.2/15.0±0.24	0.488

0.560 eV, respectively. This suggests that the two blend systems except IFL-ED-4F, which has a higher energy loss than high-efficiency blends, have room for further improving the photovoltaic performance through fine control [17,40,41].

In addition, to verify the potential of EDOT-bridged NFAs as ternary compounds, they were introduced to PM6:BTP-BO-4Cl, a high-performance combination of photovoltaic layers. As can be seen in Figs. S21a and b, it will be interesting to fabricate a ternary solar cell with a PM6 donor polymer, having a bandgap, which is similar to that of PBDB-T, because its absorption spectrum is complementary to NFAs. Furthermore, NFAs have an absorption spectrum that is highly complementary to the BTP-BO-4Cl acceptor with a 1.34 eV bandgap. Therefore, all ternary blend films cover a wide spectrum of 300 to 950 nm, which is a desirable combination for improving light harvesting and increasing photocurrent generation. The photovoltaic performance was investigated and optimized based on the conventional device structure of ITO/poly (3,4-ethylenedioxythiophene):poly(styrenesulfonate) (PEDOT:PSS)/PM6:NFAs:BTP-BO-4Cl/2,9-bis[3-[[3-(dimethylamino)propyl]amino]propyl]-anthra[2,1,9-def:6,5,10-d'e'f']diisoquinoline-1,3,8,10(2H,9H)-tetrone (PDINN)/Ag. The optimization procedures involved D1:A2:A1 ratios and thermal annealing temperatures (see Table S6). All blend films were optimized to a thickness of 100 nm. Subsequently, the most effective photovoltaic characteristics were observed when 10% of each NFA was introduced into the existing PM6:BTP-BO-4Cl 1:1 (wt/wt) blend. The optimized $J-V$ and EQE curves are shown in Fig. 3c and 3d, and the detailed parameters are listed in Table 2. First, when IFL-ED-4F was introduced into the ternary blend, it showed a PCE of 14.7% with a V_{oc} of 0.851 V, J_{sc} of 25.2 mA cm^{-2}, and FF of 68.5%, which is slightly higher than the reference efficiency (14.4% PCE with a V_{oc} of 0.838 V, J_{sc} of 24.1 mA cm^{-2}, and FF of 71.5%). When IDT-ED-4F was introduced, V_{oc} and J_{sc} increased slightly to 0.852 V and 24.9 mA cm^{-2}, respectively. However, it showed the same PCE of 14.4% owing to the relatively low FF. Finally, the blend with IDTT-ED-2F achieved the highest PCE of 15.2% with a V_{oc} of 0.849 V, J_{sc} of 25.2 mA cm^{-2}, and FF of 71.2%, unlike the results of the binary device based on PBDB-T. In summary, the performance increased in the following order: IDTT-ED-2F, IFL-ED-4F, and IDT-ED-4F. The main cause of this increased performance is that the V_{oc} values increased by approximately 0.012 to 0.014 V and the J_{sc} values increased by approximately 0.8 to 1.1 mA cm^{-2} derived from the difference in the HOMO and LUMO energy levels and the complementary optical properties between the three com-

ponents. Specifically, the calculated J_{sc} values from the integration of the EQE curves are in good agreement with the observed J_{sc} values in the $J-V$ measurement, and the deviations are within 5%. Moreover, the photovoltaic performance for NFAs-based ternary blends showed the consistently high PCEs compared to that of binary blend as shown in Fig. S22. It means that the utilizing of EDOT-based NFA as a third component is good strategy for high performance OSCs.

This high efficiency may be a result of the optimal HOMO and LUMO energy offset difference between the donor (D1) and two acceptors (A1 and A2), as well as the minimized E_{loss}, causing the charge carrier separation probability to increase [42–46]. The smallest E_g^{opt} is 1.34 eV for BTP-BO-4Cl with an onset absorption of 925 nm and eV_{oc} of 0.838, 0.851, 0.852, and 0.850 eV in the blends for PM6:BTP-BO-4Cl, PM6:IFL-ED-4F:BTP-BO-4Cl, PM6:IDT-ED-4F:BTP-BO-4Cl, and PM6:IDTT-ED-2F:BTP-BO-4Cl, respectively. Therefore, the E_{loss} values were calculated to be 0.502, 0.489, 0.488, and 0.490 eV, respectively. The E_{loss} values reported in the literature typically range from 0.7 to 1.0 eV [7,17]; thus, the introduction of EDOT-bridged NFAs would provide an increased efficiency because the E_{loss} values of 0.488 to 0.490 eV are slightly smaller than that of the reference cell. More precisely, the E_{loss} values for PM6:IFL-ED-4F:BTP-BO-4Cl, PM6:IDT-ED-4F:BTP-BO-4Cl, and PM6:IDTT-ED-2F:BTP-BO-4Cl can be calculated from the EQE curves for each device as 0.489, 0.490, and 0.488 eV, respectively, owing to the respective changed E_g^{opt} values of 1.340, 1.342, and 1.338 eV for each onset absorption. These values appear to be more consistent with the trends of the characterized photovoltaic results.

2.4. Charge transport analysis

The charge transfer properties between the donor and acceptor in all NFA-based blend films must be investigated to clarify their contribution to the device performance. Photoluminescence (PL) measurements are convenient tools for probing charge transfer or energy transfer between materials. These measurements were performed for all films of the pristine (PBDB-T, PM6, BTP-BO-4Cl, $PC_{71}BM$, IFL-ED-4F, IDT-ED-4F, and IDTT-ED-2F) and optimized (PBDB-T:IFL-ED-4F, PBDB-T:IDT-ED-4F, PBDB-T:IDTT-ED-2F, IDTT-ED-2F:$PC_{71}BM$, PM6:BTP-BO-4Cl, PM6:IFL-ED-4F:BTP-BO-4Cl, PM6:IDT-ED-4F:BTP-BO-4Cl, and PM6:IDTT-ED-2F:BTP-BO-4Cl) blends, respectively (Figs. S23–S25) [32,35,47]. Each material exhibits a pronounced PL emission in the ranges of 600 to 900 nm and 650 to 900 nm when excited at 530 nm and 630 nm, respectively. Additionally, in all blends, the PL quenching (PLQ) rates were clearly observed in the range of 700 to 850 nm. As shown in Fig. S23, for the binary blends of PBDB-T:IFL-ED-4F, PBDB-T:IDT-ED-4F, and PBDB-T:IDTT-ED-2F, the PL emissions of the donor to blend (D → B) and acceptor to blend (A → B) were partially quenched, with $PLQ_{D\rightarrow B}$s of 70.6%, 78.6%, and 44.9% and PLQ_{AB}s of 62.4%, 81.2%, and −35.5% (under excitation at 530 nm), respectively, and $PLQ_{D\rightarrow B}$ of 77.0%, 89.0%, and 46.5% and $PLQ_{A\rightarrow B}$ of 38.8%, 40.8%, and 28.9% (under excitation at 630 nm), respectively. This implies that the photoexcited charge carriers could not be effectively transferred to each counterpart material, such as PBDB-T:IDTT-ED-2F, PBDB-T:IFL-ED-4F, and PBDB-T:IDT-ED-4F. As shown in Fig. S24, IDTT-ED-2F showed much lower PLQ values when it was mixed with the $PC_{71}BM$ acceptor than with the PBDB-T donor. This demonstrates that, as in the previous device results, it is appropriate for IDTT-ED-2F to act as an electron acceptor. Specifically, these results are highly consistent with the J_{sc} values obtained from the photovoltaic results and their EQE responses, which are related to charge carrier recombination [19,32,40].

As shown in Fig. S25, all ternary blends based on EDOT-bridged NFAs showed higher PLQ values than the PBDB-T-based binary blends. This implies that they mix well with one another and charge transfer between constituent materials occurs smoothly when NFAs are introduced as the third component in the PM6:BTP-BO-4Cl combination. As shown in Fig. 4a, when A2 is introduced into the existing dominant D1:A1 blend, the cascade energy-level alignment property among the components is ideal in terms of charge transfer [42–46,48–50]. As shown in Fig. 4b, in terms of frontier energy levels, the ternary blend systems with IFL-ED-4F and IDT-ED-4F mostly have good energy level alignment properties. However, they have reversed HOMO offsets between A2-A1 and between D1-A2, respectively, which can induce charge recombination such as "hole back" transfer. In contrast, the ternary blend based on IDTT-ED-2F allows efficient charge transfer to occur by forming a good cascade energy-level alignment between the HOMO and LUMO levels of each component [15,49,50]. As a result, more interestingly, the PL of IDTT-ED-2F-based ternary blend can be considerably quenched by each other, indicating that exciton dissociations are the highest efficient among the ternary systems, as shown in Fig. 4c. Notably, the maximum PLQ_{DB} → and $PLQ_{A\rightarrow B}$ values for PM6:IDTT-ED-2F:BTP-BO-4Cl were slightly higher than those of PM6:BTP-BO-4Cl, wherein the values were 93.5% and 85.7% ($PLQ_{D\rightarrow B}$) and 90.8% and 79.6% ($PLQ_{A\rightarrow B}$), respectively, under excitation at 530 nm. These results are in good agreement with the HOMO and LUMO offsets and energy loss, which supports the results of the photovoltaic parameters for each optimized device. The detailed values are presented in Tables S7 and S8.

In addition, we measured the space-charge-limited current (SCLC) of the hole-only and electron-only devices to verify the charge carrier transport properties of the binary and ternary optimized devices for PBDB-T:IFL-ED-4F, PBDB-T:IDT-ED-4F, PBDB-T:IDTT-ED-2F, PM6:BTP-BO-4Cl, PM6:IFL-ED-4F:BTP-BO-4Cl, PM6:IDT-ED-4F:BTP-BO-4Cl, and PM6:IDTT-ED-2F:BTP-BO-4Cl (Fig. S26) [32,47]. The results of hole and electron mobilities (μ_h and μ_e) and their balance (μ_h/μ_e) were calculated and summarized using the modified Mott–Gurney equation shown in Table S9. In short, the binary blend devices demonstrated lower hole and electron mobilities (6.58×10^{-5} to 1.68×10^{-4} $cm^2\ V^{-1}\ s^{-1}$ for μ_hs and 1.02×10^{-6} to 9.18×10^{-5} $cm^2\ V^{-1}\ s^{-1}$ for μ_es) and poorer charge transport balances (1.71 to 64.51) than those of the other devices based on PBDB-T [8,9,11,17]. This may be due to the relatively weak exciton dissociation properties revealed by PL measurements. Considering the ternary system based on PM6:BTP-BO-4Cl, the devices introduced by three different components (IFL-ED-4F, IDT-ED-4F, and IDTT-ED-2F) showed similar or slightly higher charge transport properties (μ_h: 2.13–3.77 $\times10^{-4}$ $cm^2\ V^{-1}\ s^{-1}$, μ_e: 3.78–5.07 $\times10^{-4}$ $cm^2\ V^{-1}\ s^{-1}$, and μ_h/μ_e: 0.44–0.74) when compared to that of PM6:BTP-BO-4Cl (μ_h: 3.35×10^{-4} $cm^2\ V^{-1}\ s^{-1}$, μ_e: 4.58×10^{-4} $cm^2\ V^{-1}\ s^{-1}$, and μ_h/μ_e: 0.73). Notably, the lowest charge transport properties were observed when IDTT-ED-2F was used as a binary component, while the highest performance was achieved when IDTT-ED-2F was used as a small portion of the ternary component. These results imply that IDTT-ED-2F in the ternary blend system effectively facilitates charge transport and extraction, which is consistent with previous data [42–46,48–50].

2.5. Morphology analysis

The morphology of the active layer is important for device performance, as it affects charge transport and collection [1,11,15,43,47,51]. Therefore, the surface morphologies of the optimized blends for PBDB-T:IFL-ED-4F, PBDB-T:IDT-ED-4F, PBDB-T:IDTT-ED-2F, PM6:BTP-BO-4Cl, PM6:IFL-ED-4F:BTP-BO-4Cl, PM6:IDT-ED-4F:BTP-BO-4Cl, and PM6:IDTT-ED-2F:BTP-BO-4Cl were investigated using atomic force microscopy (AFM), as shown in Fig. 5. All blend films were prepared under the same conditions as those used for the optimized device fabrication.

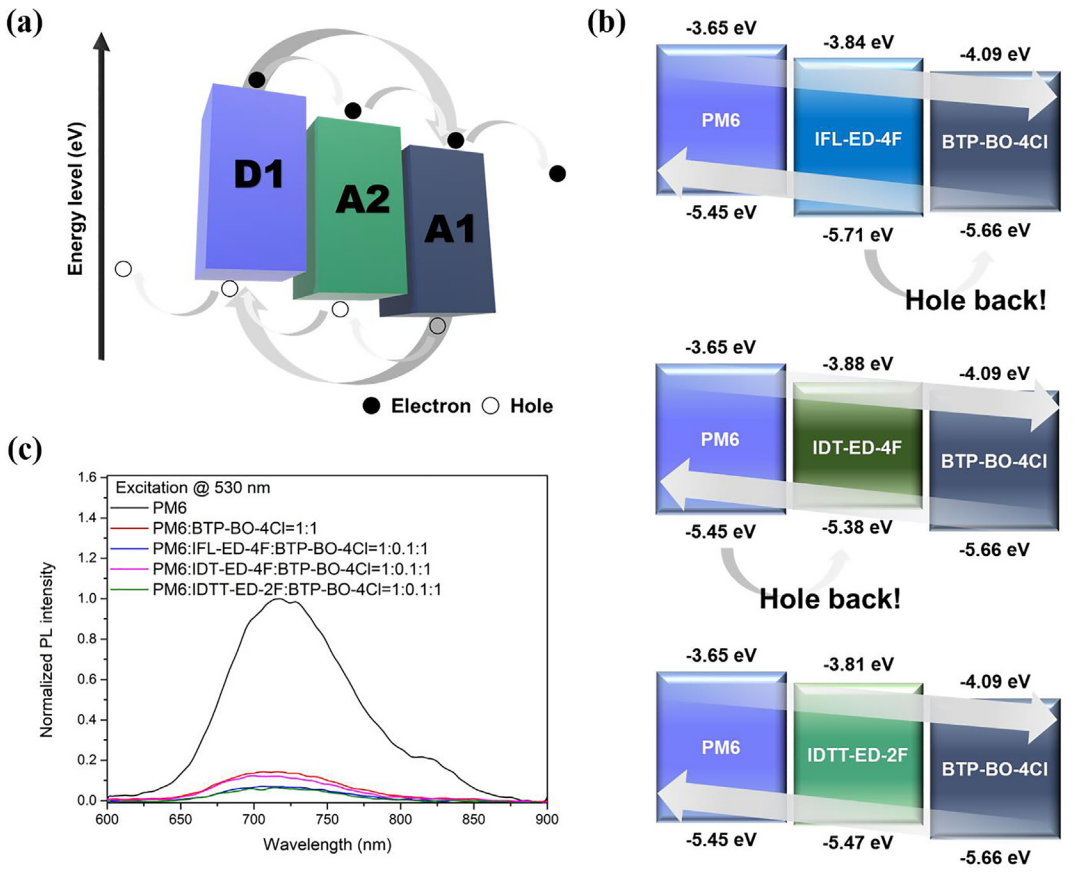

Fig. 4. (a) Ideal charge transfer mechanism diagram of a ternary blend system based on the D1:A2:A1 blend; the arrows indicate the possible pathway of charge carrier transfer and transport. (b) Energy-level band diagram for ternary blend systems of PM6:IFL-ED-4F:BTP-BO-4Cl, PM6: IDT-ED-4F, and PM6:IDTT-ED-2F in this study. (c) Photoluminescence (PL) spectra for the pristine film of PM6 and optimized blend films of PM6:BTP-BO-4Cl, PM6:IFL-ED-4F:BTP-BO-4Cl, PM6:IDT-ED-4F:BTP-BO-4Cl, and PM6:IDTT-ED-2F:BTP-BO-4Cl (excited at 530 nm).

As seen from the height images, the binary blend films demonstrated increasingly smooth and fine morphologies in the order of PBDB-T:IFL-ED-4F, PBDB-T:IDT-ED-4F, and PBDB-T:IDTT-ED-2F. More specifically, as shown in the phase images, large aggregates were observed in PBDB-T:IFL-ED-4F and PBDB-T:IDTT-ED-2F. This resulted in root-mean-square (RMS) roughness values of 1.88 and 2.10 nm, respectively, and maximum roughness profile height (R_z) of 17.21 and 30.79 nm, respectively, thereby suppressing efficient charge carrier transport and increasing charge recombination [35,52]. As shown in Fig. S27, IDTT-ED-2F:$PC_{71}BM$, which demonstrated an efficiency lower than 1% owing to its extremely low charge transfer property, formed a fully separated phase morphology without mixing, which resulted in a very high RMS and R_z of 5.78 nm and 26.67 nm, respectively. The PBDB-T:IDT-ED-4F film with a $\geq$ 10% efficiency showed the lowest RMS (1.76 nm) and R_z (12.57 nm), but the surfaces of relatively bright parts were aggregated at the microscale. These morphologies may lead to a higher probability of charge recombination before free charges can reach the donor–acceptor interface, thereby resulting in a poor performance [47,51].

In contrast, in the case of the ternary blends based on NFAs, all films showed relatively smooth and uniform features, such as the reference film for PM6:BTP-BO-4Cl. When the EDOT-bridged NFAs were introduced to PM6:BTP-BO-4Cl, they increased slightly to 1.93, 1.73, and 1.71 nm for RMS and 15.04, 20.03, and 16.20 nm for R_z compared to the reference (1.68 nm and 13.43 nm). Therefore, the surface roughness of PM6:IFL-ED-4F and PM6:IDT-ED-4F, which have relatively high RMS and R_z values, can make it difficult to form defect-free contact with PDINN/Ag, resulting in decreased FF values [25]. Among the ternary blends, the topography of PM6:IDTT-ED-2F:BTP-BO-4Cl showed relatively nanoscale bicontinuous phase separation by donor–acceptor interpenetrating networks, which are beneficial for exciton dissociation and charge transport [2,50]. In particular, as shown in the phase images, the introduction of IDTT-ED-2F produced more distinct fibrillar features of nanometer sizes, which can cause high J_{sc} values owing to the enhanced charge transport characteristics [42,45]. To investigate the in-depth film morphology, transmission electron microscopy (TEM) measurements for ternary blend of PM6:IDTT-ED-2F:BTP-BO-4Cl with binary blend of PM6:BTP-BO-4Cl were performed as shown in Fig. S28. From TEM images, the binary blend of PM6:BTP-BO-4Cl exhibit the homogeneous and interpenetrating networks with fine phase morphology. When adding the IDTT-ED-2F component to the PM6:BTP-BO-4Cl, the ternary blend film shows a distinct nanoscale phase-separated morphology with fibril structures, which is in favor of enhanced charge generation and transport. However, when further IDTT-ED-2F with amount of 20% is introduced into the PM6:BTP-BO-4Cl blend, large aggregated islands are formed on the phase surface as shown in Fig. S29. This can cause a low FF by increasing the charge carrier recombination [53,54]. These results match well with the parameters of the photovoltaic devices, PL, and SCLC.

2.6. Molecular orientation and crystallinity analysis

To better understand the nanoscale structures (crystallinity and molecular orientations) of the pristine NFAs and optimized blend films, X-ray diffraction (XRD) measurements of out-of-plane (OOP) and in-plane (IP) views of all films were conducted; the results obtained are shown in Figs. 6 and S30

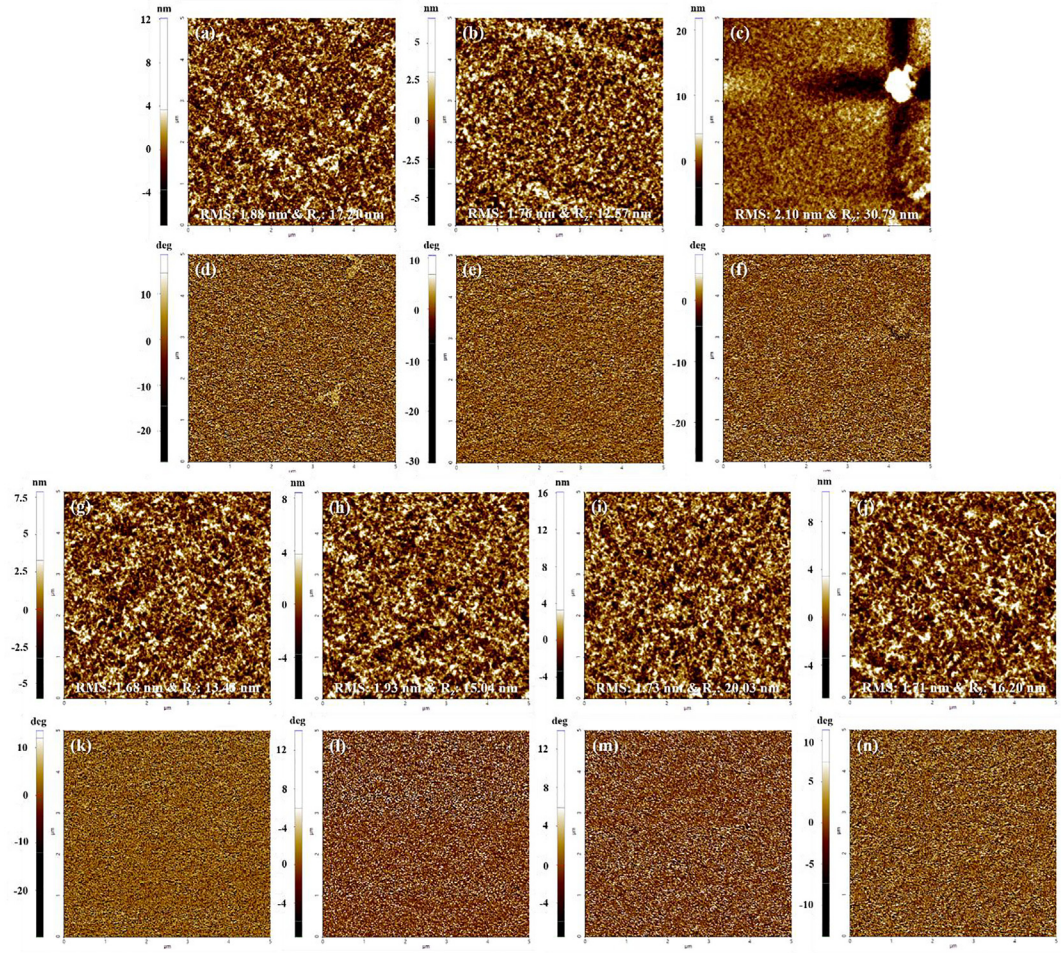

Fig. 5. AFM height (a–c, g–j) and phase (d–f, k–n) images (5 μm × 5 μm) for optimized blends: (a, d) PBDB-T:IFL-ED-4F, (b, e) PBDB-T:IDT-ED-4F, (c, f) PBDB-T:IDTT-ED-2F, (g, k) PM6:BTP-BO-4Cl, (h, l) PBDB-T:IFL-ED-4F:BTP-BO-4Cl, (i, m) PBDB-T:IDT-ED-4F:BTP-BO-4Cl, and (j, n) PBDB-T:IDTT-ED-2F:BTP-BO-4Cl.

[21,26,33,40,43,47,50]. All films were compared and analyzed by exclusively considering the major crystal peaks. As shown in Fig. 6a, when the OOP and IP directions were examined together, the pristine films of IFL-ED-4F, IDT-ED-4F, and IDTT-ED-2F showed dominant edge-on, face-on, and face-on structures, respectively. More specifically, IFL-ED-4F showed a long-range order with strong lamellar peaks at 2θ = 4.98°, 7.76°, and 11.44° [33,51]. IDT-ED-4F appears to be nearly amorphous, but as shown in Fig. S30a, a peak showing the π − π stacking property was observed at approximately 25.7°. In particular, the face-on structure of the IDT-ED-4F film with relatively weak crystallinity was verified by additional analysis using two-dimensional grazing-incidence wide-angle X-ray scattering (2D-GIWAXS) with a high-energy X-ray beam (Fig. S31) [10,11,33,51]. IDTT-ED-2F with a D-π-A structure, which is the only asymmetric structure, showed a wide amorphous region of 15° to 20° and the strongest π − π stacking property among the three NFAs [33,35].

As shown in Fig. 6b, each NFA combined with the PBDB-T polymer with good lamellar packing properties showed rapid changes in the crystal and orientation properties. First, PBDB-T:IDT-ED-4F, which showed a high efficiency of > 10%, formed efficient intermolecular charge transport channels in both the vertical and horizontal directions owing to its strong lamellar structures and π − π stacking properties [10,34,50]. By contrast, the long-range

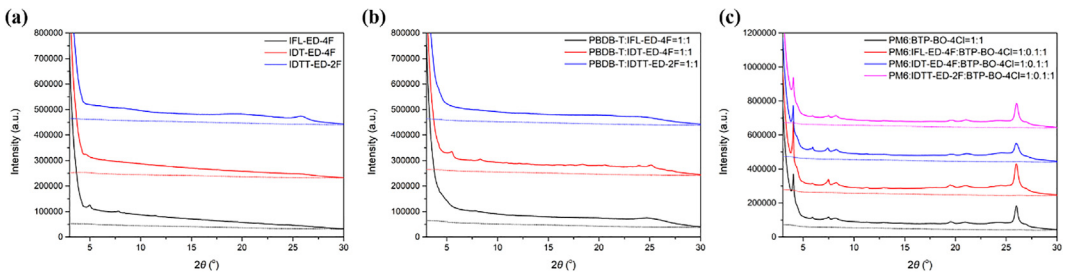

Fig. 6. X-ray diffraction profiles for the (a) pristine EDOT-bridged NFAs for IFL-ED-4F, IDT-ED-4F, and IDTT-ED-2F, (b) optimized binary blends for PBDB-T:IFL-ED-4F, PBDB-T:IDT-ED-4F, and PBDB-T:IDTT-ED-2F, and (c) optimized ternary blends for PM6:BTP-BO-4Cl (reference), PM6:IFL-ED-4F:BTP-BO-4Cl, PM6:IDT-ED-4F:BTP-BO-4Cl, and PM6:IDTT-ED-2F:BTP-BO-4Cl; solid line is out-of-plane and dotted line is in-plane.

Table 3
XRD results for the pristine and blend films based on NFAs in the out-of-plane direction.

Conditions	d_{l1} [Å]at 2θ [°]	d_{l2} [Å]at 2θ [°]	d_{l3} [Å]at 2θ [°]	d_{l4} [Å]at 2θ [°]	d_{l5} [Å]at 2θ [°]	$d_{\pi-\pi}$ [Å]at 2θ [°]
IFL-ED-4F	17.73at 4.98	–	11.38at 7.76	–	7.73at 11.44	–
IDT-ED-4F	19.03at 4.64	–	–	–	–	3.46at 25.70
IDTT-ED-2F	–	–	–	–	–	3.45at 25.80
PBDB-T:IFL-ED-4F = 1:1	–	–	11.38at 7.76	–	–	3.60at 24.70
PBDB-T:IDT-ED-4F = 1:1	16.05at 5.50	–	–	10.64at 8.30	–	3.55at 25.10
PBDB-T:IDTT-ED-2F = 1:1	–	–	–	–	–	–
PM6:BTP-BO-4Cl = 1:1	21.85at 4.04	14.87at 5.94	11.78at 7.50	10.88at 8.12	–	3.42at 26.00
PM6:IFL-ED-4F:BTP-BO-4Cl = 1:0.1:1	21.96at 4.02	14.92at 5.92	11.81at 7.48	10.72at 8.24	–	3.42at 26.00
PM6:IDT-ED-4F:BTP-BO-4Cl = 1:0.1:1	21.96at 4.02	14.87at 5.94	11.87at 7.44	10.77at 8.20	–	3.43at 25.96
PM6:IDTT-ED-2F:BTP-BO-4Cl = 1:0.1:1	21.85at 4.04	14.87at 5.94	11.78at 7.50	10.72at 8.24	–	3.42at 26.04

order property of IFL-ED-4F, which showed the strongest crystal property, was broken when it was mixed with PBDB-T. As a result, the peak was observed only at 7.76°, and the π − π stacking distance became longer than that of PBDB-T:IDT-ED-4F. Lastly, in the case of IDTT-ED-2F, which showed the strongest π − π stacking, the intrinsic orientation properties disappeared completely when it was mixed with PBDB-T, thereby forming an amorphous phase. This implies that IDTT-ED-2F is too mixed with PBDB-T polymers, which can cause poor photovoltaic characteristics [51].

In contrast, as shown in Fig. 6c, the introduction of EDOT-bridged NFAs into PM6:BTP-BO-4Cl as the third component effectively improved the crystal and orientation properties in most cases. The reference film, PM6:BTP-BO-4Cl, showed six distinct peaks at 4.04°, 5.94°, 7.50°, 8.12°, 12.88°, and 26.0°, thus exhibiting both long-range ordering and high π–π stacking properties [12]. In particular, it was confirmed to have complementary crystal and orientation properties with BTP-BO-4Cl based on the fact that the peaks of the PM6 polymer near 4° and 12° were maintained and the peak near 25° was strengthened, as shown in Fig. S32 [12,42]. First, the introduction of IFL-ED-4F with strong crystallinity slightly increased the d-spacing distances of the 4° and 7.5° lamellar peaks, but the lamellar crystallinity of these peaks and the π–π stacking property of 26° improved simultaneously. This may have improved the J_{sc} value [21,26,33,40,43]. Next, it can be seen that in PM6:IDT-ED-4F:BTP-BO-4Cl, the overall packing order properties were weakened as the intensity of the crystals decreased at the five peaks of the same position except at 5.94°. This can be associated with the relatively low J_{sc} value of the ternary-blend-based photovoltaic devices examined above. Lastly, the ternary blend with face-on dominant IDTT-ED-2F showed almost the same orientation characteristics as those of the reference. However, the crystal size increased relatively at 8.24° and the π–π stacking distance became closer to 26.04°, thus achieving the highest photovoltaic efficiency. The d-spacing (d_{ln}; wherein ln is a lamellar crystal peak discovered *n*th from the low angle) and π–π stacking ($d_{\pi-\pi}$) distances for the XRD results were calculated using the 2θ value in the equation of Bragg's law ($\lambda = 2d\sin\theta$; Cu, λ = 1.541 Å; *d*: distance) and are summarized in Table 3. These results suggest that EDOT-bridged NFAs are important for adjusting the crystal and orientation properties as ternary elements for the efficient fabrication of OSCs.

2.7. Investigation of IDTT-ED-2F as a universal third component

To further study the universality of IDTT-ED-2F as a third component in other photoactive systems, choosing a binary system with optical and electrochemical properties complementary to those of the third component is important. Thus, PM6:BTP-eC9 and PTB7-Th:IEICO-4F were selected as the main components enabling cascade energy-level alignments with IDTT-ED-2F (Fig. S33) [55,56]. However, in the case of the ternary blend of PTB7-Th:IDTT-ED-2F:IEICO-4F, the HOMO offset between the IDTT-ED-2F and IEICO-4F is slightly reversed (by 0.03 eV). Therefore, if the driving force is insufficient, the charge recombination will be high. The detailed photovoltaic performance is shown in Fig. S34 and Tables S10 and S11. In summary, both ternary blend devices for PM6:IDTT-ED-2F:BTP-eC9 and PTB7-Th:IDTT-ED-2F:IEICO-4F exhibit higher PCEs of 16.0% and 11.8%, respectively, compared to that of each reference cell (15.2% and 11.5%). Notably, these improvements are due to the V_{oc} and J_{sc} being simultaneously enhanced by introducing IDTT-ED-2F. To understand the photovoltaic results between binary and ternary blends, E_{loss} values were investigated from each EQE onset of the fabricated devices, as shown in Fig. S35. In the case of devices based on PM6:BTP-eC9, the ternary blend had a smaller E_{loss} (0.431 eV) compared to that of the binary blend (0.471 eV); thus, it showed efficient charge separation and a large increase in efficiency. Next, although the performance of the ternary device based on PTB7-Th:IDTT-ED-2F:IEICO-4F increased slightly, E_{loss} was calculated to be 0.535 eV, which is similar to that obtained with PTB7-Th:IEICO-4F (0.541 eV). This relatively small improvement could mainly be attributed to energy-level mismatches, such as HOMO offset between both acceptors. These results demonstrate the significant potential of asymmetric D-π-A EDOT-bridged NFAs being utilized for high-performance OSCs in the near future if the photoactive components satisfy the energy-level alignment.

3. Conclusion

EDOT is an attractive material as a π-bridge for developing efficient NFAs that form noncovalent conformational locking between adjacent units, thus enabling a highly planar backbone, effective reduction of the bandgap, and formation of an upshifted LUMO level. In this study, three EDOT-bridged NFAs for IFL-ED-4F, IDT-ED-2F, and IDTT-ED-2F were successfully synthesized and simultaneously demonstrated low bandgaps (1.67, 1.42, and 1.49 eV, respectively) and upshifted LUMO levels (-3.88, −3.84, and −3.81 eV, respectively). Unfortunately, the NFAs were not efficient in binary blends based on PBDB-T in terms of photovoltaic performance. However, when they were used as the third component in ternary blends based on PM6:BTP-BO-4Cl, they achieved the same or higher efficiency than the reference by assisting the optical and electrochemical properties between the two substances and simultaneously increasing V_{oc} and J_{sc}. In particular, our study suggests a few crucial guidelines for the efficient utilization of EDOT bridges in the molecular design of A-π-D-π-A building blocks. First, to achieve a highly planar backbone, a material that is flanked by heterocyclic rings at both terminals of the D core should be selected. Second, to achieve a high yield and purity, R2, a synthetic route with a relatively low synthetic complexity, should be selected instead of R1, which is the typical synthetic route. Finally, as demonstrated by their high efficiency when used as the ternary elements of the D-π-A-type IDTT-ED-2F, the potential of EDOT-

bridged NFAs should be explored through new combinations of different materials such as D-π-A or A-D-π-A.

Declaration of Competing Interest

The authors declare that they have no known competing financial interests or personal relationships that could have appeared to influence the work reported in this paper.

Acknowledgments

This paper was supported by the KU Research Professor Program of Konkuk University, the Korea Institute of Energy Technology Evaluation and Planning (KETEP) and the Ministry of Trade, Industry & Energy (MOTIE) of the Republic of Korea (No. 20193091010110), and a National Research Foundation of Korea (NRF) grant funded by the Korean government (MSIT) (No. 2020R1A2C201091611).

Appendix A. Supplementary data

Supplementary data to this article can be found online at https://doi.org/10.1016/j.jechem.2021.05.032.

References

[1] A.J. Heeger, Adv. Mater. 26 (2014) 10–28.
[2] L. Lu, T. Zheng, Q. Wu, A.M. Schneider, D. Zhao, L. Yu, Chem. Rev. 115 (2015) 12666–12731.
[3] F. Zhang, O. Inganäs, Y. Zhou, K. Vandewal, Natl. Sci. Rev. 3 (2016) 222–239.
[4] S. Mukherjee, X. Jiao, H. Ade, Adv. Energy Mater. 6 (2016) 1600699.
[5] J. Liu, S. Chen, D. Qian, B. Gautam, G. Yang, J. Zhao, J. Bergqvist, F. Zhang, W. Ma, H. Ade, O. Inganäs, K. Gundogdu, F. Gao, H. Yan, Nat. Energy 1 (2016) 16081.
[6] J. Hou, O. Inganäs, R.H. Friend, F. Gao, Nat. Mater. 17 (2018) 119–128.
[7] J. Zhang, H.S. Tan, X. Guo, A. Facchetti, H. Yan, Nat. Energy 3 (2018) 720–731.
[8] Y. Lin, J. Wang, Z.G. Zhang, H. Bai, Y. Li, D. Zhu, X. Zhan, Adv. Mater. 27 (2015) 1170–1174.
[9] W. Zhao, D. Qian, S. Zhang, S. Li, O. Inganäs, F. Gao, J. Hou, Adv. Mater. 28 (2016) 4734–4739.
[10] J. Yuan, Y. Zhang, L. Zhou, G. Zhang, H.L. Yip, T.K. Lau, X. Lu, C. Zhu, H. Peng, P.A. Johnson, M. Leclerc, Y. Cao, J. Ulanski, Y. Li, Y. Zou, Joule 3 (2019) 1140–1151.
[11] J. Yuan, Y. Zhang, L. Zhou, C. Zhang, T.K. Lau, G. Zhang, X. Lu, H.L. Yip, S.K. So, S. Beaupré, M. Mainville, P.A. Johnson, M. Leclerc, H. Chen, H. Peng, Y. Li, Y. Zou, Adv. Mater. 31 (2019) 1807577.
[12] G. Zhang, X.K. Chen, J. Xiao, P.C.Y. Chow, M. Ren, G. Kupgan, X. Jiao, C.C.S. Chan, X. Du, R. Xia, Z. Chen, J. Yuan, Y. Zhang, S. Zhang, Y. Liu, Y. Zou, H. Yan, K.S. Wong, V. Coropceanu, N. Li, C.J. Brabec, J.L. Bredas, H.L. Yip, Y. Cao, Nat. Commun. 11 (2020) 3943.
[13] L. Perdigón-Toro, H. Zhang, A. Markina, J. Yuan, S.M. Hosseini, C.M. Wolff, G. Zuo, M. Stolterfoht, Y. Zou, F. Gao, D. Andrienko, S. Shoaee, D. Neher, Adv. Mater. 32 (2020) 1906763.
[14] Y. Firdaus, V.M. Le Corre, J.I. Khan, Z. Kan, F. Laquai, P.M. Beaujuge, T.D. Anthopoulos, Adv. Sci. 6 (2019) 1802028.
[15] A. Karki, A.J. Gillett, R.H. Friend, T.Q. Nguyen, Adv. Energy Mater. 65 (2020) 2003441.
[16] G.P. Kini, S.J. Jeon, D.K. Moon, Adv. Mater. 32 (2020) 1906175.
[17] C. Yan, S. Barlow, Z. Wang, H. Yan, A.-K.-Y. Jen, S.R. Marder, X. Zhan, Nat. Rev. Mater. 3 (2018) 18003.
[18] H. Wang, J. Cao, J. Yu, Z. Zhang, R. Geng, L. Yang, W. Tang, J. Mater. Chem. A 7 (2019) 4313–4333.
[19] Z. Zhang, W. Liu, T. Rehman, H.X. Ju, J. Mai, X. Lu, M. Shi, J. Zhu, C.Z. Li, H. Chen, J. Mater. Chem. A 5 (2017) 9649–9654.
[20] Y. Liu, C. Zhang, D. Hao, Z. Zhang, L. Wu, M. Li, S. Feng, X. Xu, F. Liu, X. Chen, Z. Bo, Chem. Mater. 30 (2018) 4307–4312.
[21] P. Jiang, S. Ming, Q.Q. Jia, Y. Liu, H. Lu, M. Li, X. Xu, H.B. Li, Z.J. Bo, J. Mater. Chem. A 6 (2018) 21335–21340.
[22] N. Zengin, H. Burhan, A. Şavk, H. Göksu, F. Şen, Sci. Rep. 10 (2020) 12758.
[23] Y.W. Han, S.J. Jeon, H.S. Lee, H. Park, K.S. Kim, H.-W. Lee, D.K. Moon, Adv. Energy Mater. 9 (2019) 1902065.
[24] K.K. Liu, X. Xu, J.L. Wang, C. Zhang, G.Y. Ge, F.D. Zhuang, H.J. Zhang, C. Yang, Q. Peng, J. Pei, J. Mater. Chem. A 7 (2019) 24389–24399.
[25] J. Yao, B. Qiu, Z.G. Zhang, L. Xue, R. Wang, C. Zhang, S. Chen, Q. Zhou, C. Sun, C. Yang, M. Xiao, L. Meng, Y. Li, Nat. Commun. 11 (2020) 2726.
[26] S. Furukawa, T. Yasuda, J. Mater. Chem. A 7 (2019) 14806–14815.
[27] D. Liu, B. Kan, X. Ke, N. Zheng, Z. Xie, D. Lu, Y. Liu, Adv. Energy Mater. 8 (2018) 1801618.
[28] A. Mahmood, A. Tang, X. Wang, E. Zhou, Phys. Chem. Chem. Phys. 21 (2019) 2128–2139.
[29] X. Du, X. Lu, J. Zhao, Y. Zhang, X. Li, H. Lin, C. Zheng, S. Tao, Adv. Funct. Mater. 29 (2019) 1902078.
[30] Z. Zheng, H. Yao, L. Ye, Y. Xu, S. Zhang, J. Hou, Mater. Today 35 (2020) 115–130.
[31] J. Wang, H. Yao, Y. Xu, L. Ma, J. Hou, Mater. Chem. Front. 5 (2021) 709–722.
[32] S.J. Jeon, Y.W. Han, D.K. Moon, Small 15 (2019) 1902598.
[33] S.J. Jeon, Y.W. Han, D.K. Moon, A.C.S. Appl, Mater. Interfaces 11 (2019) 9239–9250.
[34] D. Li, X. Zhang, D. Liu, T. Wang, J. Mater. Chem. A 8 (2020) 15607–15619.
[35] S.J. Jeon, Y.W. Han, D.K. Moon, Sol. RRL 3 (2019) 1900094.
[36] T.D. Kim, K.S. Lee, Macromol. Rapid Commun. 36 (2015) 943–958.
[37] S. Li, L. Zhan, C. Sun, H. Zhu, G. Zhou, W. Yang, M. Shi, C.Z. Li, J. Hou, Y. Li, H. Chen, J. Am. Chem. Soc. 141 (2019) 3073–3082.
[38] H. Sun, B. Liu, J. Yu, X. Zou, G. Zhang, Y. Zhang, W. Zhang, M. Su, Q. Fan, K. Yang, J. Chen, H. Yan, F. Gao, X. Guo, Sci. China Chem. 63 (2020) 1785–1792.
[39] S. Mathew, A. Yella, P. Gao, R. Humphry-baker, B.F.E. Curchod, N. Ashari-Astani, L. Tavernelli, U. Rothlisberger, M.K. Nazeeruddin, M. Grätzel, Nature Chem. 6 (2014) 242–247.
[40] Y. Qin, S. Zhang, Y. Xu, L. Ye, Y. Wu, J. Kong, B. Xu, H. Yao, H. Ade, J. Hou, Adv. Energy Mater. 9 (2019) 1901823.
[41] A. Classen, C.L. Chochos, L. Luer, V.G. Gregoriou, J. Wortmann, A. Osvet, K. Forberich, I. McCulloch, T. Heumueller, C.J. Brabec, Nat. Energy. 5 (2020) 711–719.
[42] D. Wang, R. Qin, G. Zhou, X. Li, R. Xia, Y. Li, L. Zhan, H. Zhu, X. Lu, H.L. Yip, H. Chen, C.Z. Li, Adv. Mater. 32 (2020) 2001621.
[43] C. Zhang, S. Ming, H. Wu, X. Wang, H. Huang, W. Xue, X. Xu, Z. Tang, W. Ma, Z. Bo, J. Mater. Chem. A 8 (2020) 22907–22917.
[44] X. Ma, J. Wang, J. Gao, Z. Hu, C. Xu, X. Zhang, F. Zhang, Adv. Energy Mater. 10 (2020) 2001404.
[45] T. Liu, Z. Luo, Q. Fan, G. Zhang, L. Zhang, W. Gao, X. Guo, W. Ma, M. Zhang, C. Yang, Y. Li, H. Yan, Energy Environ. Sci. 11 (2018) 3275–3282.
[46] A. Zeng, M. Pan, B. Lin, T.K. Lau, M. Qin, K. Li, W. Ma, X. Lu, C. Zhan, H. Yan, Sol. RRL 4 (2020) 1900353.
[47] J.E. Yu, S.J. Jeon, J.Y. Choi, Y.W. Han, E.J. Ko, D.K. Moon, Small 15 (2019) 1805321.
[48] D. Su, K. Li, W. Liu, W. Zhang, X. Li, Y. Wu, F. Shen, S. Huo, H. Fu, C. Zhan, Macromol. Rapid Commun. 41 (2020) 2000393.
[49] D. Zhou, W. You, H. Xu, Y. Tong, B. Hu, Y. Xie, L. Chen, J. Mater. Chem. A 8 (2020) 23096–23122.
[50] P. Bi, X. Hao, Sol. RRL 3 (2019) 1800263.
[51] S.J. Jeon, Y.W. Han, Y.H. Kim, D.K. Moon, Sol. RRL 4 (2020) 2000074.
[52] S.J. Jeon, Y.H. Kim, D.H. Hong, N.G. Yang, Y.W. Han, D.K. Moon, Sol. RRL 5 (2020) 2000608.
[53] W. Su, Q. Fan, X. Guo, X. Meng, Z. Bi, W. Ma, M. Zhang, Y. Li, Nano Energy 38 (2017) 510–517.
[54] R. Yu, S. Zhang, H. Yao, B. Guo, S. Li, H. Zhang, M. Zhang, J. Hou, Adv. Mater. 29 (2017) 1700437.
[55] Y. Cui, H. Yao, J. Zhang, K. Xian, T. Zhang, L. Hong, Y. Wang, Y. Xu, K. Ma, C. An, C. He, Z. Wei, F. Gao, J. Hou, Adv. Mater. 32 (2020) 1908205.
[56] S. Xin, N. Gasparini, Y. Long, H. Yao, J. Hou, H. Ade, D. Baran, ACS Energy Lett. 3 (2018) 669–676.